A&A 545, C3 (2012)
DOI: 10.1051/0004-6361/201118483e

Astronomy & Astrophysics

Corrigendum

Variations on a theme – the evolution of hydrocarbon solids

III. Size-dependent properties – the optEC$_{(s)}$(a) model*

A. P. Jones[1,2]

[1] Institut d'Astrophysique Spatiale, CNRS, UMR8617, 91405 Orsay, France
[2] Université Paris Sud, IAS UMR8617, 91405 Orsay, France
e-mail: `Anthony.Jones@ias.u-psud.fr`

A&A 542, A98, DOI: 10.1051/0004-6361/201118483

Key words. dust, extinction – ISM: general – ISM: molecules – errata, addenda

In the computation of the complex refractive index data for the original published version of this article, and also in the preceding paper Jones (2012), there was an error in the calculation of the IR band intensities. This error results in small changes in the 3 μm region bands and an underestimation of the band strengths and continua at longer wavelengths for hydrogen-rich a-C:H materials ($X_{\rm H} \gtrsim 0.23 \equiv E_{\rm g} \gtrsim 1$ eV). Also, the aromatic domain cluster size distribution has been more accurately calculated for all a-C(:H) particles, resulting in a reduction in n and k at long wavelengths ($\lambda \gtrsim 0.5\,\mu$m) for small band gap materials ($E_{\rm g} \lesssim 0.25$ eV) with a = 10 and 30 nm. The conclusions of the paper are unchanged, except as indicated in the following, where an updated version of the relevant figure and, if necessary, the accompanying text is given. The section headings and figure numbers are the same as those used in the originally-published paper. The refractive index data that were originally made available through the CDS have now been replaced with corrected data.

Additionally, there was an error in the overly-complicated reasoning in the deduction of the a-C(:H) particle photo-processing time-scales in Sect. 5.2 of this paper, which was carried over from Sect. 5.1 of the preceding paper (Jones 2012). The photo-processing time-scale is simply the inverse of the photo-darkening rate, $\Lambda_{\rm UV,pd}$, given in Eq. (31) of Jones (2012). A new and modified version of Sect. 5.2, which replaces the previously published version, is given below.

4. The optEC$_{(s)}$(a) model refractive index data

Figures 3 and 4 show the updated refractive index data for 100 nm and 0.5 nm radius a-C:H particles. The most significant differences are apparent in k and occur for large band gap materials with $E_{\rm g} \gtrsim 1$ eV. The IR band strengths for $\lambda > 4\,\mu$m and the long-wavelength continua are enhanced with respect to the previous results. The real parts of the refractive indices, n, are not significantly affected.

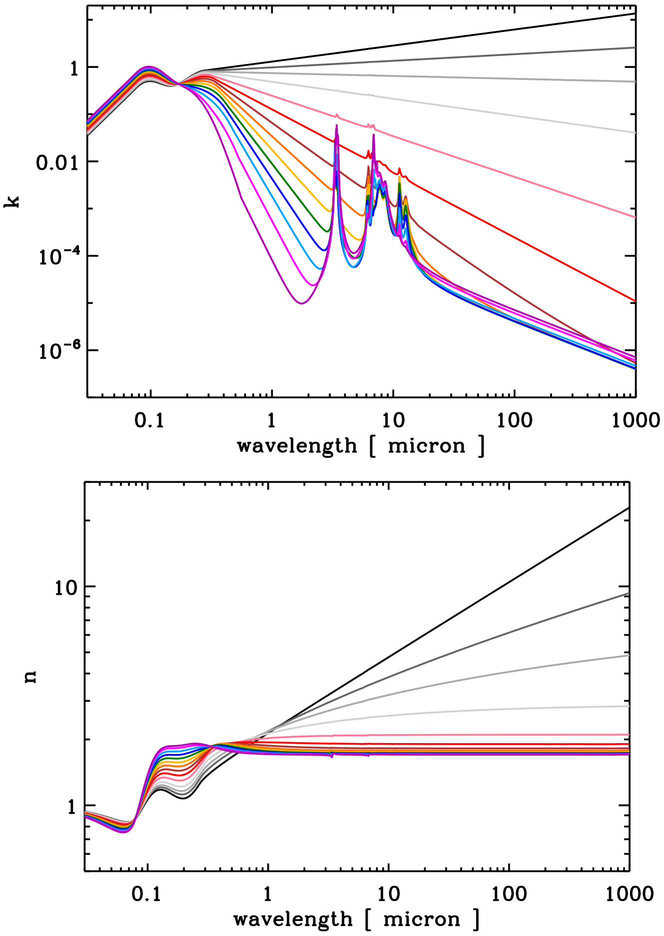

Fig. 3. The imaginary (k, *upper plot*) and real (n, *lower plot*) parts of the refractive index for 100 nm radius particles as a function of $E_{\rm g}$ for large gap (2.67 eV, lower purple lines at λ = 2 μm) to small gap (−0.1 eV, upper black lines at λ = 2 μm) a-C(:H) materials (see Table 1 for the full colour-coding scheme).

---

* Data files are only available at the CDS via anonymous ftp to `cdsarc.u-strasbg.fr (130.79.128.5)` or via
`http://cdsarc.u-strasbg.fr/viz-bin/qcat?J/A+A/545/C3`

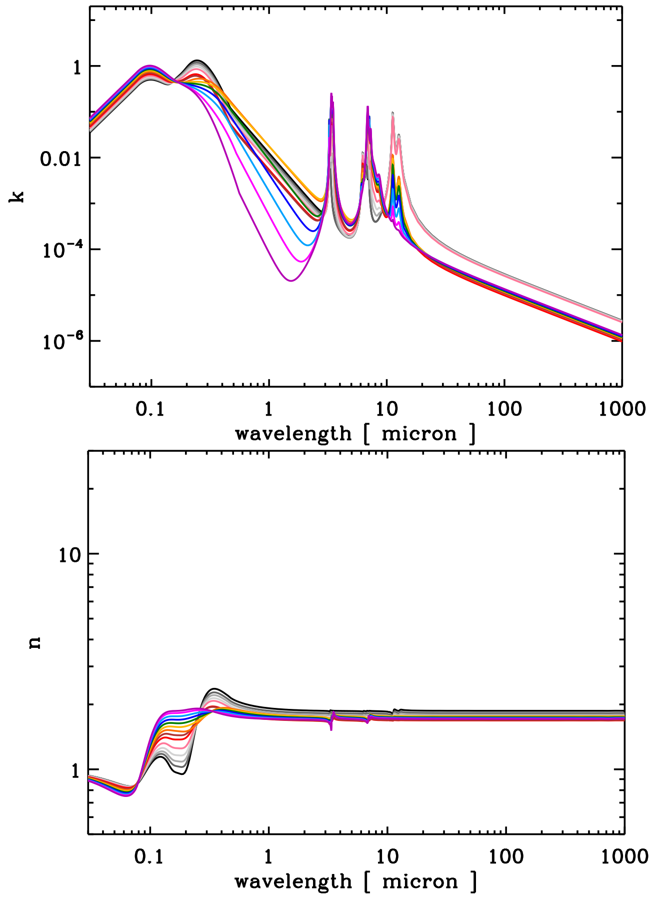

Fig. 4. Same as for Fig. 3 but for 0.5 nm radius particles. Note that, at $\lambda = 2\,\mu$m, n and k change little with size for a-C:H materials with $E_{\rm g} \geq 1.5$ eV (lower purple to yellow lines in the *upper k plot*) but bunch-up for $E_{\rm g} < 1.5$ eV. Note also that, for $\lambda > 20\,\mu$m, the n and k data appear to be almost independent of the band gap for $E_{\rm g} \geq 0.5$ eV.

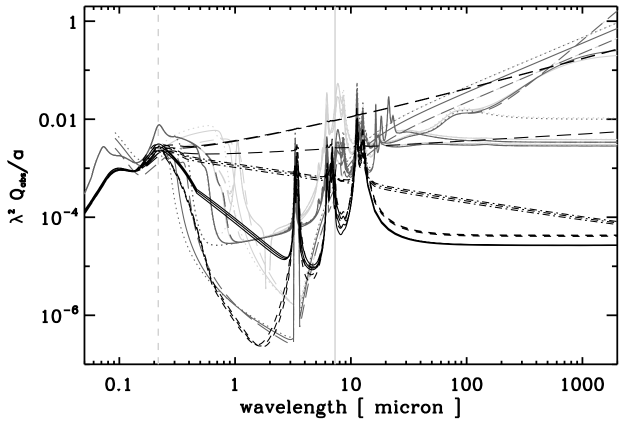

Fig. 5. $\lambda^2 Q_{\rm abs}/a$ for 0.33 nm (short-dashed), 0.5 nm (solid), 1 nm (dashed-dotted) and 3 nm (long-dashed) radius particles: for a-C(:H) with $E_{\rm g}$(bulk) = 0.5, 0.25 and 0.1 eV (black lines, from lower to upper at 100 μm) and neutral and cation PAHs with the same number of C atoms (dark and light grey solid lines, respectively, Desert et al. 1990; Draine & Li 2001, 2007; Compiègne et al. 2011). The dashed, vertical, grey line shows the peak position of the UV bump and the solid, vertical, grey line shows the upper wavelength limit for the well-constrained a-C(:H) IR features.

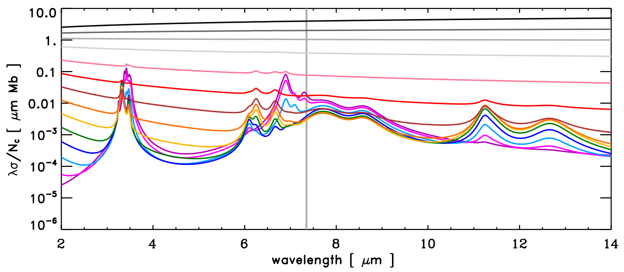

Fig. 8. The predicted spectra of optEC$_{\rm (s)}$(a)-modelled particles of radius 100 nm, presented as the wavelength times absorption coefficient per carbon atom, $\lambda\alpha/N_{\rm C}$, in the 2–14 μm region (1 Mb = 10^{-18} cm^2). Note how the spectra evolve from aliphatic-rich with prominent IR bands to aromatic-rich with no evident IR bands but a much stronger continuum. N.B. The bands with central positions long-ward of the vertical grey line ($\lambda(\nu_0) > 7.3\,\mu$m) are not yet well-determined by laboratory measurements.

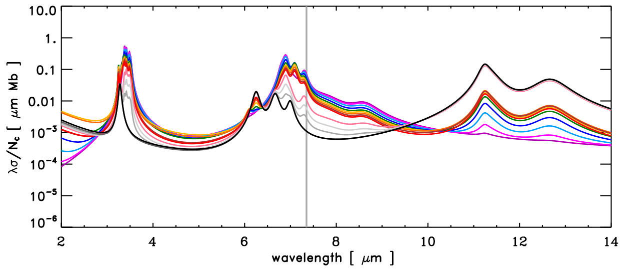

Fig. 9. As per Fig. 8 but for particles of radius 0.5 nm. Note how the spectra bunch up and how the IR band positions evolve from aliphatic-rich (with maxima in the ≈3.4 and ≈7 μm regions) to aromatic-rich (with maxima at 3.3, 6.3, 6.7, 7.0, 11.3 and 12.7 μm).

4.1. Comparison of nm-sized a-C(:H) particles with PAHs

Figure 5 now includes the updated a-C(:H) data for comparison with the interstellar PAH model data. Note that the longer wavelength IR bands are now in better agreement with the PAH IR bands in the 5–15 μm region. Also, the 0.33 nm radius a-C(:H) particle continuum is much stronger in this plot but still significantly less that that predicted by the interstellar PAH models. The properties of the larger a-C(:H) particles (0.5 nm and 1 nm radii) were not affected by the error in the IR band intensity calculations.

Thus, the critical conclusions of this comparison section remain entirely valid.

4.4. The optEC$_{\rm (s)}$(a) particle 2–14 μm spectra

The a-C(:H) cross-section data has been corrected in Figs. 8 and 9. The new data show stronger bands and continuum with respect to the previously-published data.

4.5. Size-dependent spectra from EUV to mm wavelengths

Figures 10 to 13 have been re-calculated based on the corrected complex indices of refraction for a-C(:H). The plot axis intervals are the same as in the originally-published versions in order to allow a direct comparison. The effects of the increased band strengths and the enhanced continua at long wavelengths ($\lambda \gtrsim 20\,\mu$m), in large band gap ($E_{\rm g} \gtrsim 1$ eV) a-C:H materials, are evident in these figures.

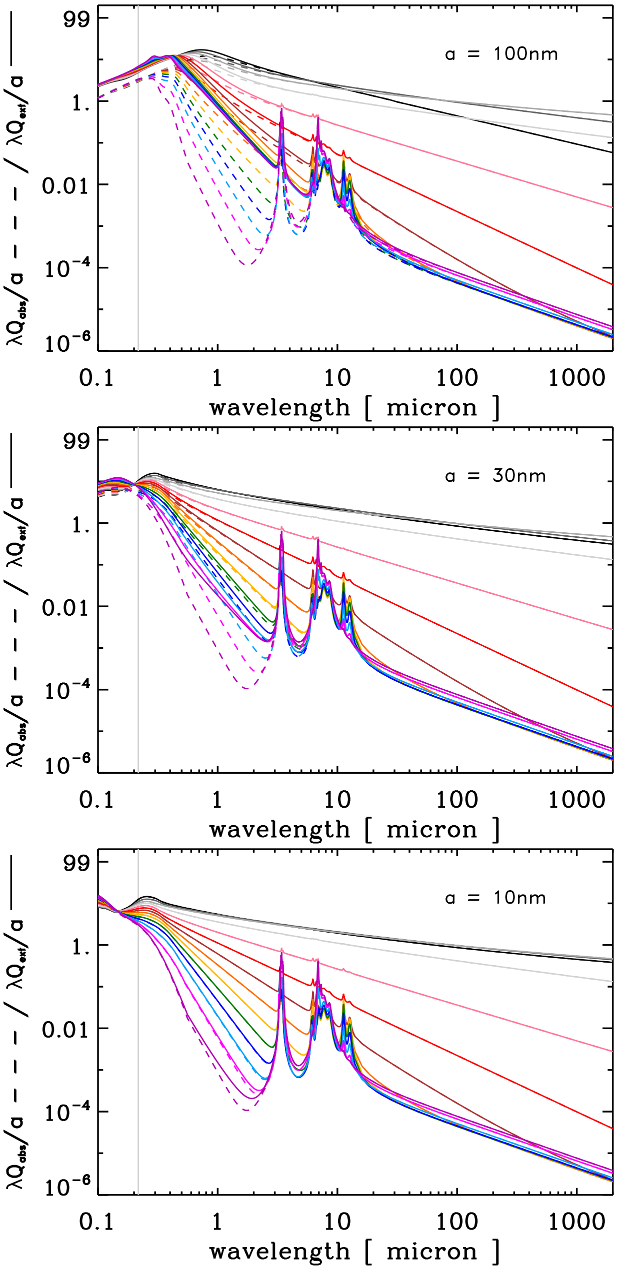

Fig. 10. $\lambda Q_{\rm ext}/a$ (solid) and $\lambda Q_{\rm abs}/a$ (dashed), for 100, 30 and 10 nm radius particles, as a function of wavelength, for all of the considered band gap materials (see Table 1). At $\lambda = 2\,\mu$m, $E_{\rm g}$ decreases from 2.67 eV (lower purple line) to −0.1 to 0.25 eV (the four upper grey and black lines). The vertical grey line marks the position of the UV extinction bump at 217 nm.

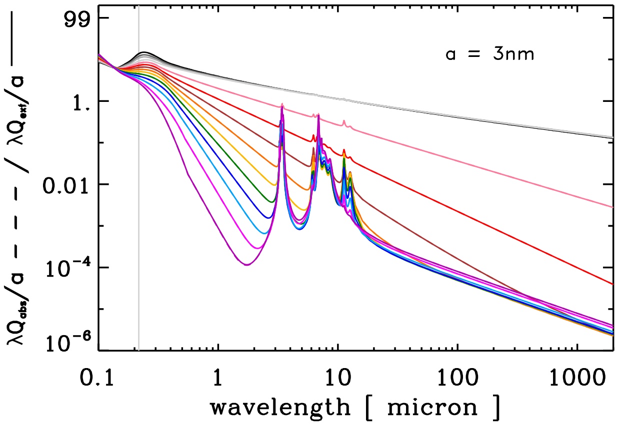

Fig. 11. Same as for Fig. 10 but for 3 nm radius particles. Note that the data for $E_{\rm g} \leq 0.25$ eV overlap for $\lambda > 1\,\mu$m.

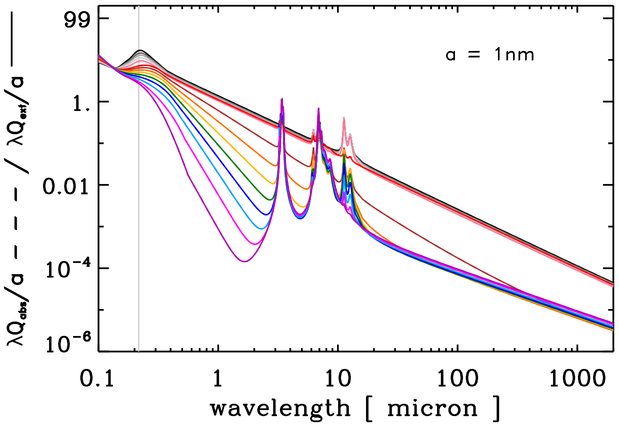

Fig. 12. Same as for Fig. 10 but for 1 nm radius particles. Note that the data for $E_{\rm g} \leq 0.75$ eV almost completely overlap for $\lambda > 1\,\mu$m.

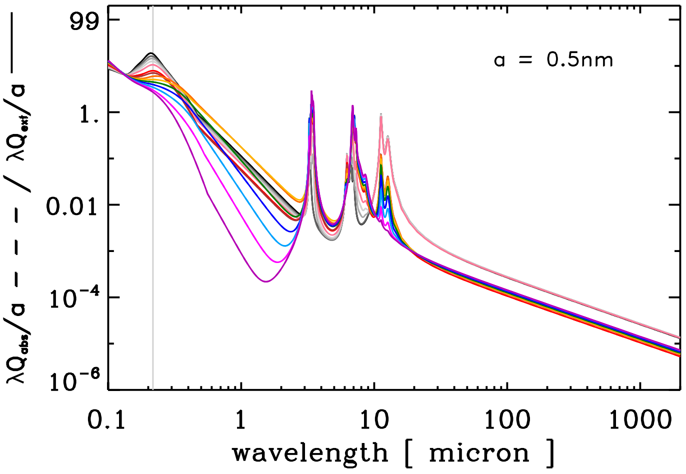

Fig. 13. Same as for Fig. 10 but for 0.5 nm radius particles. Note the bunching up of all of the data, except for the H-rich materials ($E_{\rm g} > 2$ eV) in the 0.5−3 μm region and at long wavelengths.

5.1. Structural variations and spectral properties

Figures 14 to 17 have been re-calculated using the corrected a-C(:H) data. All of the interpretations and conclusions of this section remain valid.

5.2. a-C(:H) processing timescales

The size-dependent a-C(:H) particle photo-processing timescales, $\tau_{\rm UV,pd}$, can be derived as per Eq. (31) of paper II by inserting appropriate values for the particle absorption efficiency, $Q_{\rm abs}(a, E)$, and the photo-darkening efficiency, ϵ (here we assume $\epsilon = 0.1$ but the exact value is uncertain). Figure 18 shows $\tau_{\rm UV,pd}$, multiplied by the ISRF factor G_0, as a function of particle radius for a-C(:H) materials ($E_{\rm g} = -0.1$ to 2.67 eV), where surface hydrogenation has been included. Presenting the a-C(:H) evolution in this way, Fig. 18 indicates that in the diffuse ISM ($G_0 = 1$) the photo-processing time-scales will likely be $\approx 10^5$ yr for 10−100 nm radius particles and $\gtrsim 10^6$ yr for $a \lesssim 1$ nm. These data should be scaled accordingly for

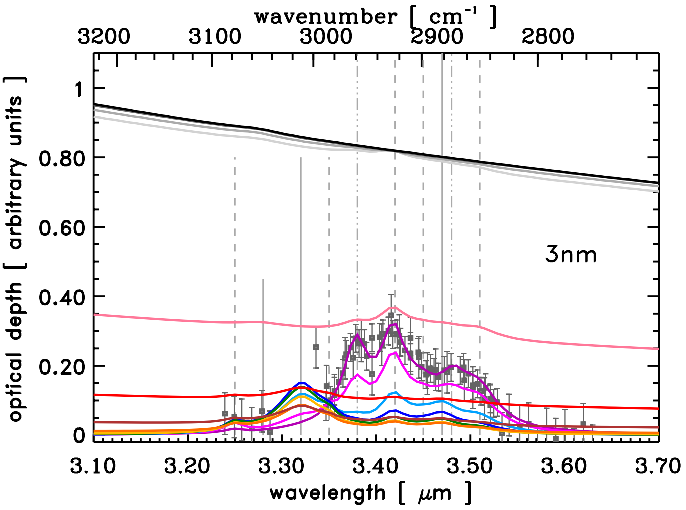

Fig. 14. The 3 μm region spectrum, presented as optical depth, for a = 3 nm a-C(:H) particles for increasing band gap, $E_g = -0.1$ to 0.25 eV (upper, grey-black), $E_g = 0.5$ eV (middle, pink), $E_g = 0.75$ eV (lower, red, y-axis intercept at ≈ 0.12) and $E_g = 1$ to 2.67 eV (lower, yellow-purple, bottom to top at $\approx 3.45\,\mu$m). The thin, grey, vertical lines indicate the band origins (see Paper I): aromatic (short), olefinic (medium) and aliphatic (long), CH (solid), CH_2 (dashed) and CH_3 (dashed-triple dotted). The data with error bars (in grey) are for the diffuse ISM line of sight towards the Galactic Centre source IRS6E and Cyg OB2 No. 12 (taken from Pendleton & Allamandola 2002). For comparison the observational data are scaled to the $E_g = 2.67$ eV data.

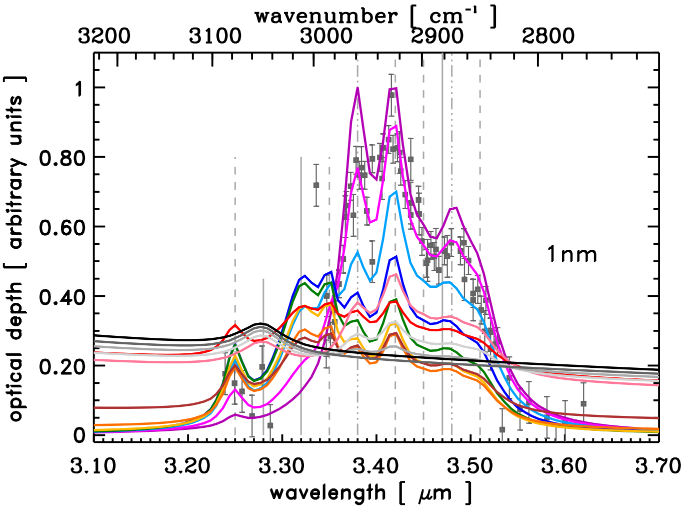

Fig. 15. Same as Fig. 14 but for a = 1 nm and for increasing band gap, E_g (−0.1 to 2.67 eV), from bottom to top at $\approx 3.45\,\mu$m. For comparison the observational data are scaled to the $E_g = 2.5$ eV data.

photo-darkening efficiencies, ϵ, other than the value of 0.1 that has been adopted here. The longer time-scales for smaller particles simply reflects their lower values of $Q_{\rm abs}(a, E)$ at UV wavelengths. Thus, it appears that all a-C(:H) particles are photo-aromatised on rather short time-scales ($\lesssim 10^6$ yr) in the ISM. However, this estimation does not include the effects of thermal processing during the stochastic heating of small a-C(:H) particles, which could be important but has not yet been evaluated. In extreme radiation field regions, i.e., photo-dissociation regions (PDRs) with $G_0 \simeq 10^3$ (10^4), the carbonaceous nano-particle photo-processing time-scales will be $\approx 10^3$ ($\approx 10^2$) yr, and it is in

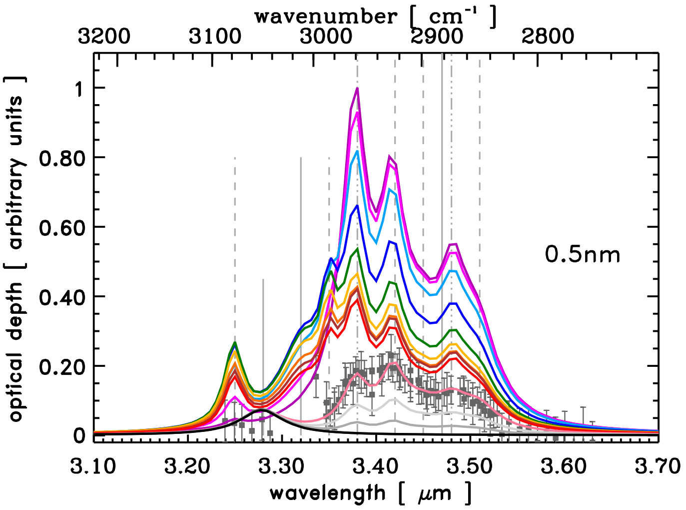

Fig. 16. Same as Fig. 14 but for a = 0.5 nm. For comparison the observational data are scaled to the $E_g = 0.5$ eV data.

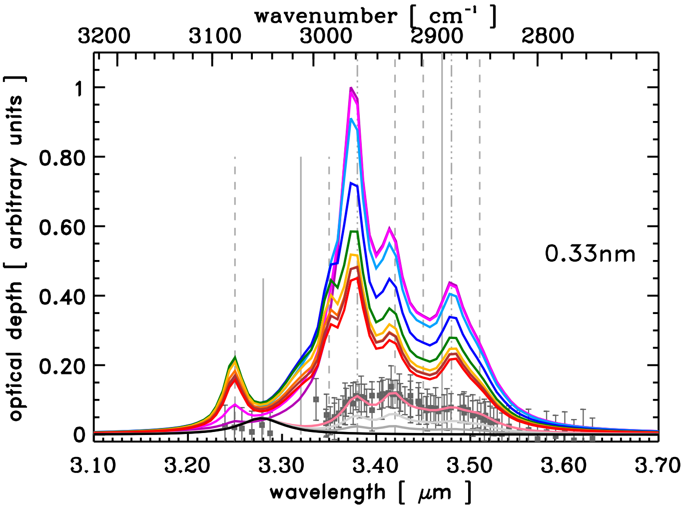

Fig. 17. Same as Fig. 14 but for a = 0.33 nm. For comparison the observational data are scaled to the $E_g = 0.5$ eV data.

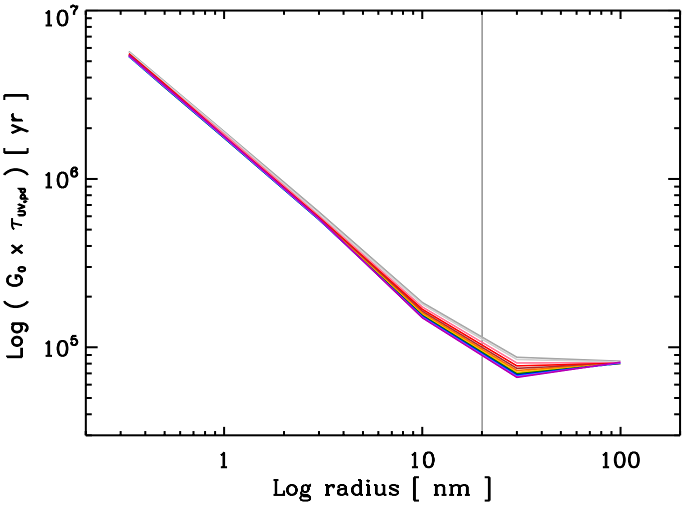

Fig. 18. a-C(:H) particle photo-processing time-scales, $\tau_{\rm UV,pd}$, multiplied by the ISRF factor G_0, as a function of particle radius for increasing band gap from top (−0.1 eV, grey) to bottom (2.67 eV, purple). A photo-darkening efficiency, $\epsilon = 0.1$, was assumed here.

such environments that the loss of aromatic emission bands is observed (Boulanger et al. 1998), thus indicating extreme carbonaceous nano-particle processing.

The effects of photo-processing and photo-darkening, the sp^3 to sp^2 transformation, resulting from exposure to ISRF UV-EUV photons, could possibly be counterbalanced by hydrogen atom addition to the structure as a result of (energetic) collisions in the interstellar medium but this possibility is not discussed here, other than to refer the reader to the discussion presented in Sect. 5.2 of Paper II.

The EUV-photolysis of a-C(:H) particles is key to their evolution in the ISM and needs to be incorporated into dust models. Carbonaceous dust evolution must therefore be treated dynamically, not only in terms of the evolution of the dust size distribution (e.g., Jones et al. 1996; Serra Díaz-Cano & Jones 2008) but also time-dependently in terms of the evolution of its chemical composition and structure (e.g., Jones 2009, Papers I and II). To this end, in the following section, provides a brief and preliminary guide to the usage of the optEC$_{(s)}(a)$ data.

5.2.1. Which optEC$_{(s)}$(a) data?

The evolution of a-C:H dust in the ISM is tied to systematic variations its band gap, E_g, which are driven by the dehydrogenating effects of extreme UV (EUV) 10−13.6 eV photon absorption (EUV-photolysis) and possibly by thermally-driven dehydrogenation during the large temperature fluctuations induced by stochastic heating following UV photon absorption.

A full investigation of the likely a-C(:H) optical properties in the ISM must await an in-depth modelling of the observed properties of carbonaceous dust in the ISM using the optEC$_{(s)}(a)$ data. However, the user is currently recommended to use the minimum band gap material for photo-processed a-C(:H) grains as indicated by the likely lower limit to the H atom fraction (viz, $X_H \simeq 0.05$) as derived by experiment (Adel et al. 1989; Marée et al. 1966; Gadallah et al. 2011; Godard et al. 2011). For the cores of larger particles, that cannot be photo-processed (i.e., at depths $\gtrsim$20 nm), the material band gap should reflect the properties of the material prior to photon-irradiation in the ISM and may be an historical vestige of the grains at their time of formation.

The required optEC$_{(s)}(a)$ model optical property data, $m(a, \lambda)$, should be chosen from those tabulated for the given radius and the required *bulk* material band gap for that radius. Note that it may be necessary to interpolate if data for the required radius or band gap, other than those tabulated, are needed. However, in this case, care will need to be exercised to ensure that the interpolated n and k data are consistent with the Kramers-Kronig relationship.

Appendix C: The size-dependent optical properties of a-C(:H) materials

The real and imaginary parts of the complex indices of refraction, n and k, respectively, in Figs. C.1 to C.5 have been corrected. Note that for the small band gap ($E_g = -0.1$ and 0 eV), 10 and 30 nm radius particles the n and k values are lower than the previously-published data because of the effects of the restricted aromatic domain sizes, which have here been calculated for the full distribution of particle-size-determined aromatic cluster sizes.

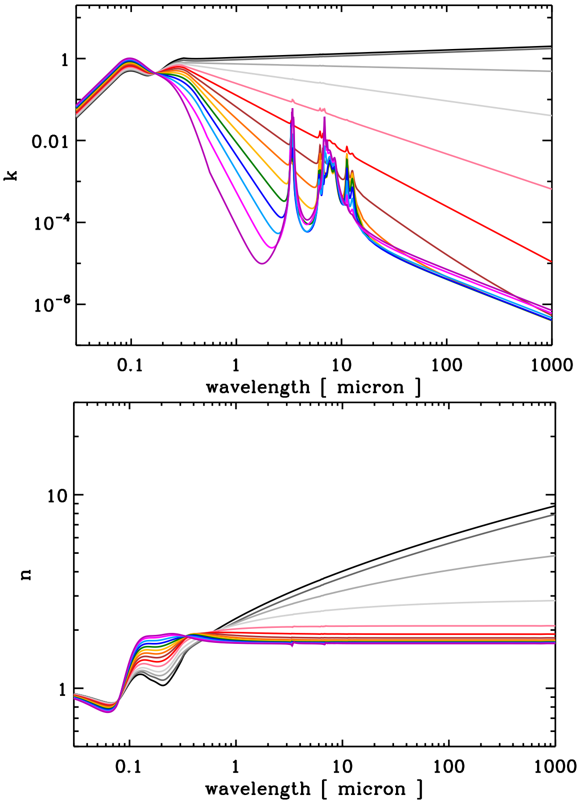

Fig. C.1. The real part, n (*upper*), and imaginary part, k (*lower*), of the complex index of refraction, $m = n(a, E_g, \lambda) + ik(a, E_g, \lambda)$, for 30 nm radius a-C(:H) particles as a function of E_g, as predicted by the optEC$_{(s)}$(a) model presented in this paper (see Table B.1 for the line colour-coding).

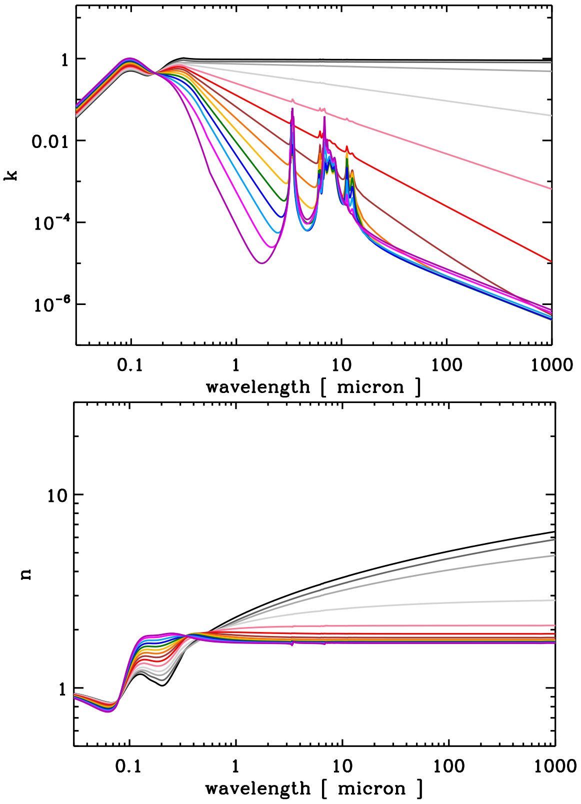

Fig. C.2. As per Fig. C.1 but for particles of radius 10 nm.

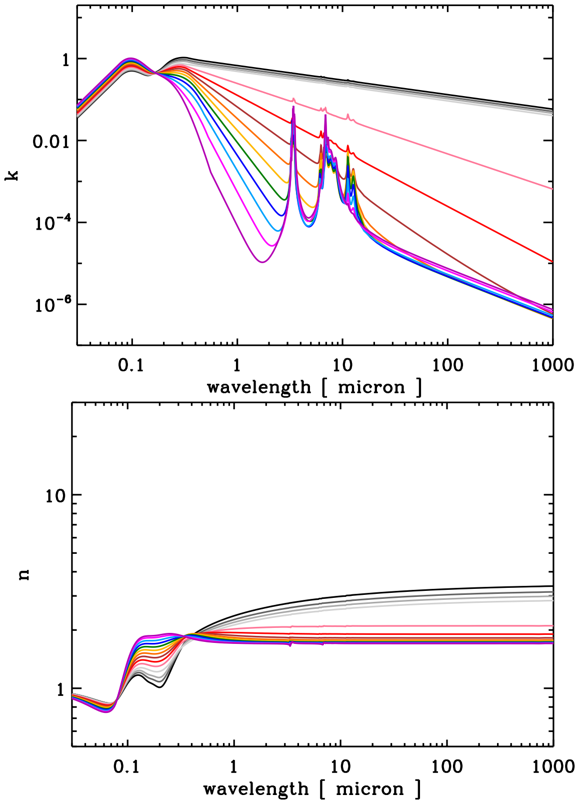

Fig. C.3. As per Fig. C.1 but for particles of radius 3 nm.

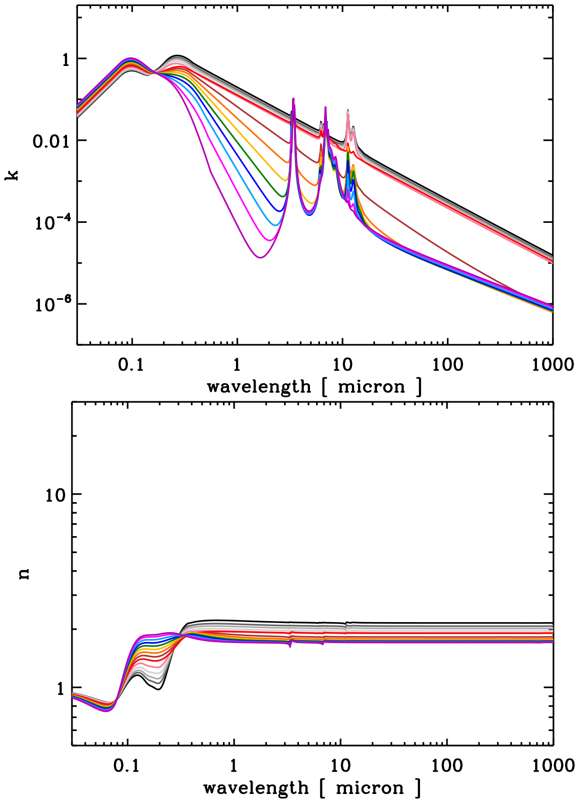

Fig. C.4. As per Fig. C.1 but for particles of radius 1 nm.

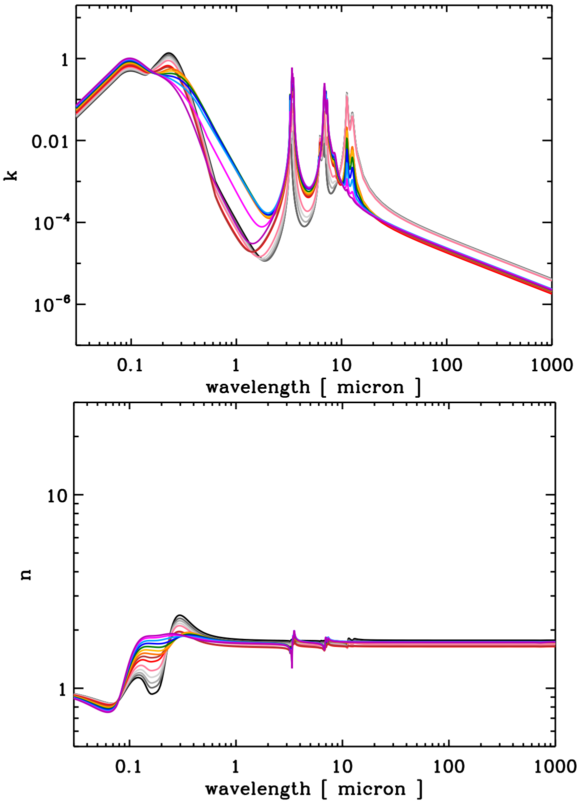

Fig. C.5. As per Fig. C.1 but for particles of radius 0.33 nm.

Appendix D: Size-dependent optical-UV properties

Figures D.2 and D.5 have been re-calculated using the new data because they do show small differences with respect to the previously published versions. All of the other figures in this Appendix are unaffected by the use of the new data.

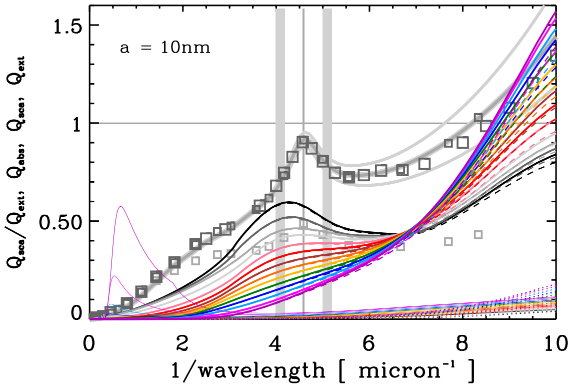

Fig. D.2. Same as for Fig. D.1 but for 10 nm radius particles. The grey squares show the diffuse ISM extinction curve for $R_V = 3.1$ (dark) and 5.1 (light) from Savage & Mathis (1979, large squares) and Mathis (1990, small squares). The grey curves indicate the average galactic extinction, and its variation (upper and lower grey curves), as derived by Fitzpatrick & Massa (2007).

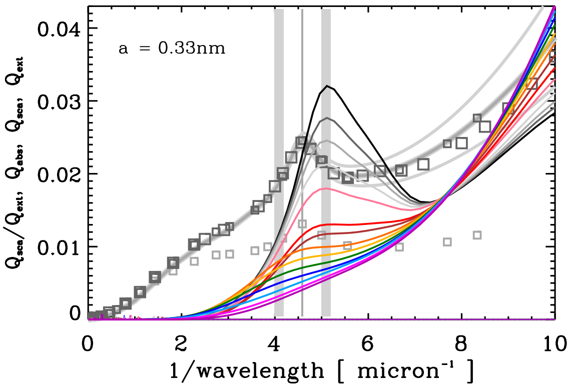

Fig. D.5. Same as for Fig. D.1 but for 0.33 nm radius particles.

Appendix E: The size-dependent spectra of optEC$_{(s)}$(a)-modelled particles

The a-C(:H) cross-section data has been corrected in Figs. E.1 to E.5. The new data show stronger bands and continuum with respect to the previously-published data.

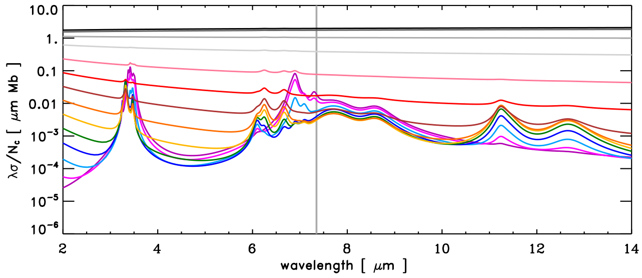

Fig. E.1. The predicted spectra of optEC$_{(s)}$(a)-modelled particles of radius 30 nm, presented as the wavelength times absorption coefficient per carbon atom, $\lambda\alpha/N_C$, in the 2–14 μm region (1 Mb = 10^{-18} cm^2). N.B. The bands with central positions long-ward of the vertical grey line ($\lambda(\nu_0) > 7.3\,\mu$m) are not yet well-determined by laboratory measurements.

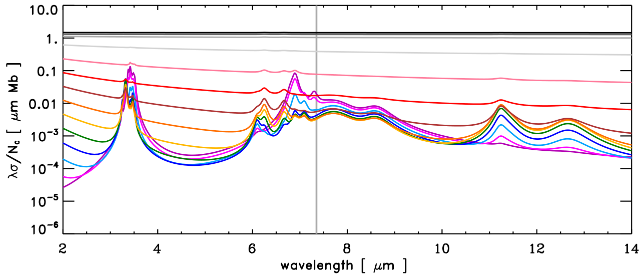

Fig. E.2. As per Fig. E.1 but for particles of radius 10 nm.

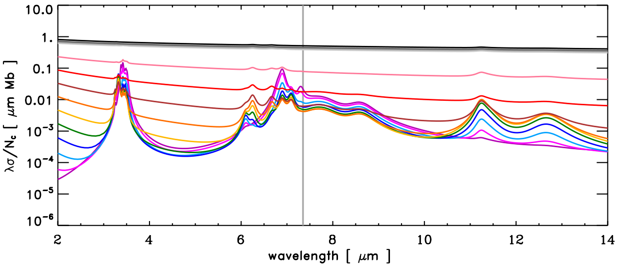

Fig. E.3. As per Fig. E.1 but for particles of radius 3 nm.

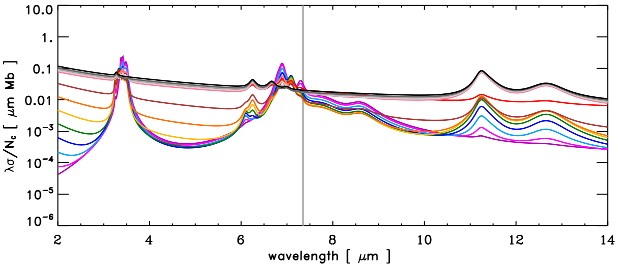

Fig. E.4. As per Fig. E.1 but for particles of radius 1 nm.

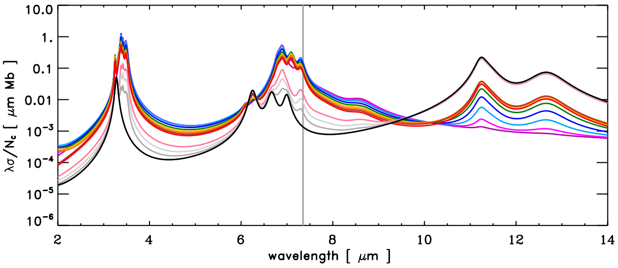

Fig. E.5. As per Fig. E.1 but for particles of radius 0.33 nm.

References

Adel, M. E., Amir, O., Kalish, R., & Feldman, L. C. 1989, J. Appl. Phys., 66, 3248
Boulanger, F., Abergel, A., Bernard, J. P., et al. 1998, in Star Formation with the Infrared Space Observatory, eds. J. Yun, & L. Liseau, ASP Conf. Ser., 132, 15
Compiègne, M., Verstraete, L., Jones, A., et al. 2011, A&A, 525, A103
Desert, F.-X., Boulanger, F., & Puget, J. L. 1990, A&A, 237, 215
Draine, B. T., & Li, A. 2001, ApJ, 551, 807
Draine, B. T., & Li, A. 2007, ApJ, 657, 810
Fitzpatrick, E. L., & Massa, D. 2007, ApJ, 663, 320
Gadallah, K. A. K., Mutschke, H., & Jäger, C. 2011, A&A, 528, A56
Godard, M., Féraud, G., Chabot, M., et al. 2011, A&A, 529, A146
Jones, A. P. 2009, in Cosmic Dust – Near and Far, eds. T. Henning, E. Grün, & J. Steinacker, ASP Conf. Ser. 414, 473
Jones, A. P. 2012, A&A, 540, A2
Jones, A. P., Tielens, A. G. G. M., & Hollenbach, D. J. 1996, ApJ, 469, 740
Marée, C. H. M., Vredenberg, A. M., & Habraken, F. H. P. M. 1966, Mat. Chem. Phys., 46, 198
Mathis, J. S. 1990, ARA&A, 28, 37
Pendleton, Y. J., & Allamandola, L. J. 2002, ApJS, 138, 75
Savage, B. D., & Mathis, J. S. 1979, ARA&A, 17, 73
Serra Díaz-Cano, L., & Jones, A. P. 2008, A&A, 492, 127